Fabrication of a positional brain shift phantom through the utilization of the frozen intermediate hydrogel state

Matthew R. Potts [a,*], Nicholas J. Bennion [a], Stefano Zappalá [b], David Marshall [b], Rob Harrison [c], Sam L. Evans [a]

[a] *School of Engineering, Cardiff University, Cardiff, UK*
[b] *School of Computer Science and Informatics, Cardiff University, Cardiff, UK*
[c] *Renishaw Plc, Miskin, UK*

ARTICLE INFO

ABSTRACT

Synthetic models (phantoms) of the brain-skull system are useful tools for the study of surgical events that are otherwise difficult to study directly in humans. To date, very few studies can be found which replicate the full anatomical brain-skull system. Such models are required to study the more global mechanical events that can occur in neurosurgery, such as positional brain shift. Presented in this work is a novel workflow for the fabrication of a biofidelic brain-skull phantom which features a full hydrogel brain with fluid-filled ventricle/fissure spaces, elastomer dural septa and fluid-filled skull. Central to this workflow is the utilization of the frozen intermediate curing state of an established brain tissue surrogate, which allows for a novel moulding and skull installation approach that permits a much fuller recreation of the anatomy. The mechanical realism of the phantom was validated through indentation testing of the phantom's brain and simulation of the supine to prone brain shift event, while the geometric realism was validated through magnetic resonance imaging. The developed phantom captured a novel measurement of the supine to prone brain shift event with a magnitude that accurately reproduces that seen in the literature.

1. Introduction

The brain is a soft deformable structure that has a small capacity to shift around within the cranial cavity. This movement is known as brain shift and has particular relevance in high precision neurosurgery (HPN). This is because HPN procedures typically rely on preoperatively planned surgical trajectories relative to the skull and, therefore, any movement of the brain inside the skull between the preoperative imaging of the patient and the delivery of instruments can lead to targeting error and, as a result, sub-optimal clinical outcomes.

Gravitational shifting of the brain within the surgically unopened cranial cavity is known as positional brain shift (PBS) and forms one of the many sources of targeting error in HPN. Unlike some of the other sources of brain shift (e.g. fluid loss upon skull opening) PBS has received little attention. This is partly due to the difficulty of imaging human subjects in non-supine positions with magnetic resonance (MR) imaging (MRI) and the more general unsuitability of computerised tomography (CT) imaging due to radiation exposure, especially in studies that require multiple sequential scans. To date, only a handful of MR and CT imaging studies have investigated PBS (Thulin et al., 1972; Hill et al., 1998; Rice et al., 2013; Schnaudigel et al., 2010; Monea et al., 2012; Mikkonen and Laakso, 2019; Ji et al., 2004; Ji and Margulies, 2007; Zappalá et al., 2021), and of these studies, only a small number of positional transitions have been looked at. These studies, however, repeatedly show that patient repositioning alone can be sufficient to induce clinically significant brain shift (>1 mm). Therefore, it is important to characterise PBS across the entire spectrum of possible positional transitions in HPN.

When a particular event is difficult to characterise *in vivo* it is often useful to turn to synthetic or computational models. Yet, while models have been produced to study other neurosurgical brain shift events, such as pneumocephalus mediated brain shift (PMBS) (Skrinjar et al., 2002; Sun et al., 2014; Forte et al., 2018) or craniotomy mediated brain shift (CMBS) (Clatz et al., 2003; Hu et al., 2007; Bilger et al., 2011), no models have been produced for the study of PBS. To address this, at Cardiff University two complimentary projects have been underway to

develop a pair of synthetic and computational (Bennion et al., 2022) models. This is in addition to a third project which seeks to develop better methods to characterise PBS *in vivo* with MRI (Zappalá et al., 2021). This present contribution focuses on the design, fabrication and validation of the synthetic model (phantom).

Unlike in the computational domain, very few phantoms of the brain-skull system exist. This is undoubtedly due to the incredible complexity of the brain-skull system and the difficulty of recreating the system with contemporary manufacturing technologies. Here, the core difficulty is that contemporary fabrication methods cannot currently replicate the body's ability to progressively differentiate and grow tissues *in situ*, which is the biological process which builds the geometrically and mechanically complex material system of the human head. To recreate the brain-skull system with available methods, we must first build individual parts from a limited selection of available material surrogates and then assemble them together.

Considering this difficulty, it is understandable why brain shift/deformation phantoms are generally designed with the minimum complexity necessary to facilitate the investigation for which they are developed, presenting for the most part as either isolated brain parts (Reinertsen and Collins, 2006; Puzrin et al., 2005; Mohammadi et al., 2015; Chen et al., 2010, 2013; Navarro-Lozoya et al., 2019) or brain simulant filled skulls (Ma et al., 2010; DeLorenzo et al., 2007). Two notable exceptions to this are the brain-skull phantoms by Bayer et al. (2018) and Forte et al. (2016) (Fig. 1), which both represent a much closer approximation of the full anatomical system than others which can be found in the literature. The notable difference with these phantoms is that they not only include a full brain and skull, but also the mechanically important space between them, the subarachnoid space (SAS). This space is critical in reproducing PBS as, without it, the large strains that have been measured to take place at its surface cannot take place (Zappalá et al., 2021).

However, while complex in their design, the phantoms by Bayer et al. and Forte et al. are still not quite suitable for PBS simulation. The phantom by Bayer et al. was developed to help validate a method for intraoperative brain shift compensation and, as such, comprised polyurethane brain (with fluid inflatable ventricles, tumours and blood vessels) and ceramic composite skull. The first issue with this phantom is that, unlike brain tissue, the polyurethane material is not poroelastic and so incapable of reproducing the large, sponge-like, volumetric strains the brain undergoes upon loading (Zappalá et al., 2021). The second is that, while containing a SAS, the space was not filled with a fluid of appropriate density to reproduce the buoyancy force that acts on the brain.

The phantom by Forte et al., on the other hand, was developed to demonstrate the utility of a novel brain tissue material surrogate in simulating CMBS and, as such, comprised composite hydrogel (CH) brain and fluid-filled plastic skull. This phantom paired a mechanically realistic brain with a fluid-filled SAS, but included a more rudimentary recreation of the brain's geometry and dural septa, with no internal cavities or complete fissure spaces, features which can influence the dynamics of brain shift (Chen et al., 2011). The skull of the phantom was also incomplete, with a large hole at the top to represent the hole that is temporarily made in the skull during craniotomy surgery. This may seem like a trivial element to change in repurposing a phantom for a different area of investigation, however, specific features and fabrication workflows are necessary to facilitate the assembly of a robustly sealed brain-skull model. This is especially the case in a model that needs to be rotated around and placed in different positions.

Yet, it should be noted that the hydrogel developed by Forte et al. presents as one of the most closely matched simulants to brain tissue, capturing both the rate dependent loading and relaxation behaviour of the tissue, whilst also presenting as a material with a reasonable density (1.015 g/cm^3) (Forte et al., 2018) and high strain to failure. This triad of properties is unique and critical for the assembly of any realistic brain-skull phantom. A high strain to failure, for example, is required if any moulded brain is to survive the extracranial handling involved in placing it into a tight fitting skull, while the loading behaviour and density influence the configuration the phantom brain will adopt in its natural, gravity-loaded state.

The present contribution focuses on the design, fabrication and validation of a novel PBS simulating brain-skull phantom, named the Cardiff University Brain Shift (CUBS) Phantom. Taking advantage of the intermediate frozen state in the formation process of the CH developed by Forte et al., we designed and used a series of moulds, parts and workflows for the assembly of a geometrically and mechanically realistic (biofidelic) phantom comprising hydrogel brain (inc. Imaging beads) with water-filled ventricle cavity, elastomer dural septa, water-filled SAS, and plastic skull. The objective of this study was to produce a full-scale biofidelic phantom capable of accurately reproducing the PBS event. This objective is met through MR imaging of the phantom's geometry, indentation testing of the phantom's brain and simulation of the supine to prone PBS event with CT based brain shift measurement.
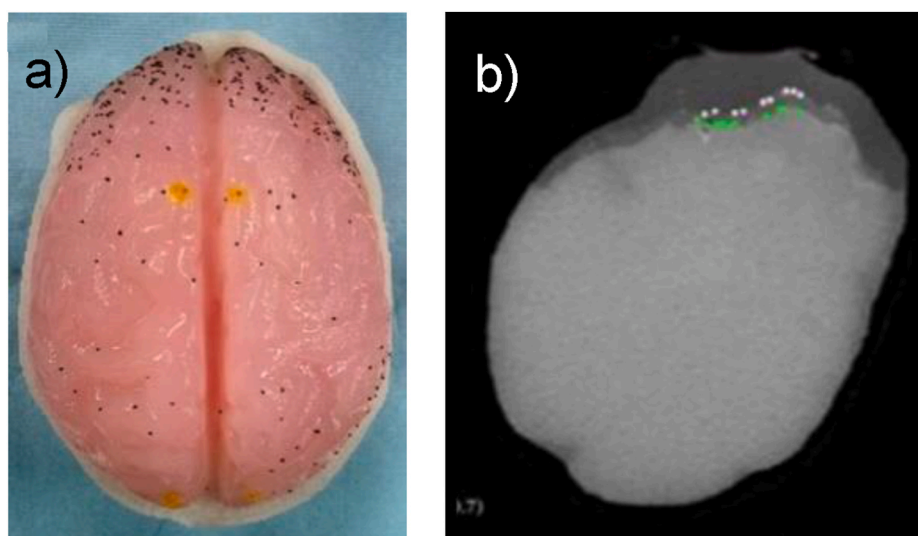

Fig. 1. Phantom developed by Forte et al. (2016). a) top down view of phantom; b) MRI scan of the phantom. Both images were adapted from Forte et al. (2016) which is covered by a creative commons license.

2. Materials and methods

2.1. Anatomical geometry acquisition

The parts described in this work were all designed in Rhino V5 using anatomical geometries segmented from an averaged MRI dataset of 152 brains: the MNI ICBM152 Average Brain Stereotactic Model (McConnell Brain Imaging Centre, Montreal Neurological Institute, McGill University) (ICBM 152 Nonlinear atlases version, 2009). This dataset was selected such that the typical anatomy could be recreated. Three structures were segmented: the brain (with ventricular and major fissure spaces), the dural septa (comprising falx cerebri, cerebellar tentorium and tentorium cerebelli) and the skull. Further information on the segmentation process is provided in Appendix 1.

2.2. Brain fabrication

2.2.1. Overview

The CH material developed by Forte et al. is a tuneable hydrogel comprised of polyvinyl alcohol (PVA), phytagel (PHY) and deionised water (Di H_2O). Like pure PVA hydrogels, the CH is formed through the freeze-thaw method, which involves the freezing of a prepared solution of the polymers down to approximately $-25\ ^\circ C$ and the subsequent thawing of the material back up to room temperature. This process results in a dual network hydrogel (Forte et al., 2016).

An unexplored benefit of this tissue surrogate (and all freeze-thaw hydrogels) is the frozen intermediate state that occurs during its formation workflow. Unlike the incredibly fragile formed state of other brain tissue surrogates, this intermediate state is strong and rigid and, therefore, can be successfully retrieved from considerably more complex mould cavities. Considering this, a novel composite brain mould (CBM) was designed and fabricated.

This mould comprised two expandable silicone halves (cast in CS25 silicone - Easy Composites, UK), five plastic tentorial inserts (3D printed in DuraForm Pa - 3D Systems, DE), one sacrificial ice ventricle insert (cast with an additional mould described later) and two locating bands (DuraForm Pa) (Fig. 2). Here, the silicone halves provide for the moulding of the majority of the brain's shape, while also providing the necessary expansive capacity of the mould (to accommodate the freeze-thaw expansion of the material). The five plastic inserts and sacrificial ice ventricle then slot into the upper and lower silicone halves to provide for the moulding of the external fissure and internal ventricular spaces of the brain, while the locating bands are used to locate the two major mould halves together. This arrangement allows for the brain to be cast, frozen and retrieved whilst still in its rigid frozen state, before being transferred to a supportive water bath for thawing (Fig. 3). When

thawed, the inserts can be removed/melted to produce a hydrogel brain complete with fissure and ventricle spaces.

A central part of the phantom's development was in tuning the formulation of the CH to work with this altered thawing method in brain production. This was required as the mechanical properties of freeze-thaw PVA hydrogels are dependent on thawing rate and the thawing protocol deviated significantly from that described by Forte et al. Indeed, brains produced with the [3.00% PVA: 0.43% PHY: 96.57% Di H_2O] CH formulation identified by Forte et al. were found to be unrealistically stiff (see Section 2.4) during the development of the methods described here. In this work, mechanical testing data and brain shift measurement is provided for two brains produced with a bespoke formulation of the CH termed the sugar formulation (SF), comprising [2.15% PVA: 0.25% PHY: 2.45% Sugar: 95.15% Di H_2O], which was identified, following an iterative development process, as producing brains with suitable mechanical properties for positional brain shift simulation (see Section 2.4). The production of these phantom brains are described in full in the next section.

2.2.2. Fabrication workflow

Phantom brain fabrication began with the preparation of the SF, which itself began with the separate production of PVA: Di H_2O and PHY: Di H_2O solutions, using PVA (146 000–186 000 molecular weight, 99+% hydrolysed) and PHY acquired from Sigma Aldrich (UK), and Di H_2O obtained from an in-house filtration system.

The PVA solution was created by adding 44 g of PVA to 975.4 g of vigorously stirring deionised water, heated to approximately $90\ ^\circ C$, and mixing for 2 h. The PHY solution, on the other hand, was created by first slowly adding 5.2 g of PHY to 975.4 g of vigorously stirring deionised water (at $20\ ^\circ C$) to avoid clumping of the powder, before progressively heating the mixture to approximately $70\ ^\circ C$ for 2 h. The SF was then created by combining the two solutions into a plastic container, together with 50.2 g of white granulated sugar (99% sucrose). This combined solution was then further mixed without heating until the solution reached room temperature. The container was finally refrigerated to approximately $5\ ^\circ C$ overnight to chill the solution close to freezing, such that, when cast the next day, the solution froze quickly around the CBM's ice ventricle insert (instead of melting it). This marked the completion of the day-before preparation of the SF solution.

Like the solution preparation, the CBM was also prepared the day before brain casting. This began with the fabrication of the ice ventricle insert, which consisted of a plastic DuraForm socket (which slots into the CBM), a plastic DuraForm stem (which slots into the socket) and a frozen Di H_2O head which was moulded onto the stem using a two-part silicone mould (cast in Mould Max 14NV silicone - Smooth On, US). This mould comprised two halves (and a locating band), with a tunnel running

Fig. 2. Assembled lower (left) and upper (right) mould halves. Silicone mould components are grey in colour, rigid plastic inserts are off-white in colour and ice ventricle insert is the clouded structure in the middle of the left hand picture. Visible are also the brain shift imaging markers (glass beads) which are supported in the cavity with cantilevered map pins and gap-bridging fishing line (see Section 2.2.2).
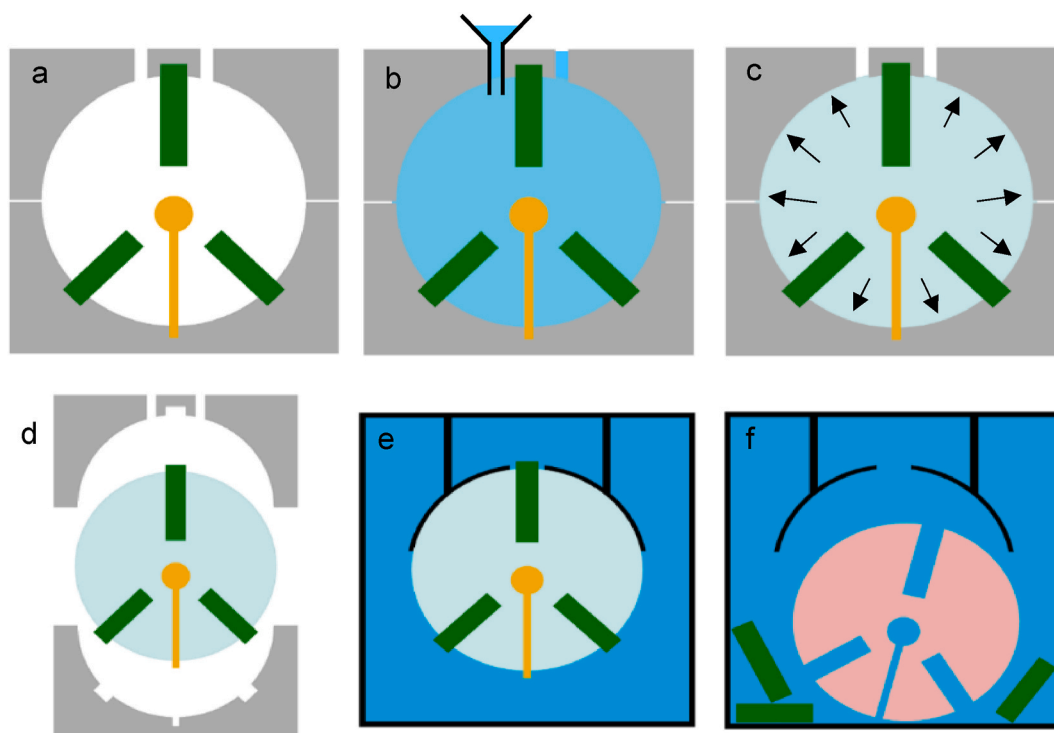
Fig. 3. Brain fabrication workflow. a) assembled composite mould comprising expandable silicone halves (grey), rigid fissure inserts (green) and ice ventricle insert (yellow); b) mould filled with hydrogel solution (blue); c) frozen mould with expanded frozen hydrogel solution (light blue); d) removal of frozen hydrogel together with trapped inserts; e) frozen hydrogel (light blue) with trapped inserts centered in bucket of water (blue); f) thawed hydrogel (pink) with freed/melted fissure and ventricle spaces.

through the bottom section that accepts the DuraForm stem (Fig. 4). When it is locked in its correct position and the mould is fully assembled, the stem then projects into the cavity, allowing for the water to freeze around it when cast though a hole at the top.

In fabricating the ice ventricle insert, the mould was first assembled and left in a −25 °C freezer for 2 h for it to acclimatise to the freezer's temperature. After freezing the mould, Di H_2O was next cast inside with the mould still in the freezer and left to freeze overnight.

Following this process, the two halves of the CBM were next prepared. This was achieved by inserting the remaining DuraForm inserts into their respective halves and positioning 44 glass bead markers (4 mm in diameter) throughout the two mould half cavities to enable the imaging of brain shift with CT. These markers were positioned using a system of map pins (cantilevered off the mould walls) and fishing lines (bridging between mould walls) (Fig. 2) which were anchored into small tunnels drilled into the mould walls. These were drawn out of the brain later when the brain was in its frozen state, leaving behind just the beads embedded in the frozen material (Fig. 5a–c). The next step, however, involved the placement of the two assembled mould halves in the freezer for overnight freezing to −25 °C.

With all pre-casting preparations completed, brain casting began the following morning. First, the ice ventricle insert was extracted from its mould and slotted into its plastic socket, which itself was inserted into the lower CBM half day before. The two halves were then assembled together within the freezer. Next, the hydrogel solution container was removed from its refrigerator and placed into an ultrasound bath, where the container's contents were then subjected to simultaneous agitation through ultrasound and a whisking motion (introduced with a pistol drill and whisk attachment) for approximately 5 min. Following this, the CH solution, still at approximately 5 °C, was poured into the mould (with the mould still sitting in the freezer). A heavy plate was next placed on top of the mould (to promote radial expansion of the cavity) before leaving the mould to freeze down to approximately −25 °C over 24 h, as specified by Forte et al. (2016) for the freezing of the CH

solution, but with 6 h extra freezing time to account for the larger size of the mould.

At the end of the freezing period, the top half of the mould was lifted off of the frozen brain, leaving behind its portion of the now trapped inserts (Fig. 5a and b). Undesirable seams were then chiselled off and the fishing line/map pins were drawn out of the brain, leaving behind only the embedded beads.

The frozen brain with trapped inserts was next placed in a thawing cap (Fig. 5c), which acted to centralize the frozen brain in an 8 L bucket for thawing. This bucket was filled moments prior with 6.5 L of refrigerated (approximately 5 °C) deionised water. The entire apparatus was next placed into a 10 °C incubator for 24 h to slowly thaw the brain (Fig. 5d). At the end of the thawing period the fissure inserts were pulled away from the now soft brain and the plastic stem of the ice ventricle insert was then drawn out via its self-moulded tract in the brain (acting as the fourth ventricle). This marked the completion of the brain's fabrication (Fig. 6).

2.3. Phantom fabrication

2.3.1. The dural septa and skull parts

In order to produce a faithful recreation of the relationship between the phantom's brain, dural septa and skull, a mechanism needed to be devised for their co-location and attachment. For this, a system was designed in which the dural septa would first be attached to the brain, followed then by the attachment of the resulting complex to the skull.

A dural septa part was designed and subsequently 3D printed in the DuraForm Flex material, which has a nominal tensile elastic modulus of 7.4 MPa (DuraForm Flex material data sheet, 2020). This is only approximately a tenth of the anatomical stiffness, however, since the part was artificially thickened to aid fabrication, a similar overall structural stiffness was likely to have been achieved. As shown in Fig. 7, the part features tabs for the attachment to the skull and a "lace-up" system down the falx portion which enables the scythe like geometry to
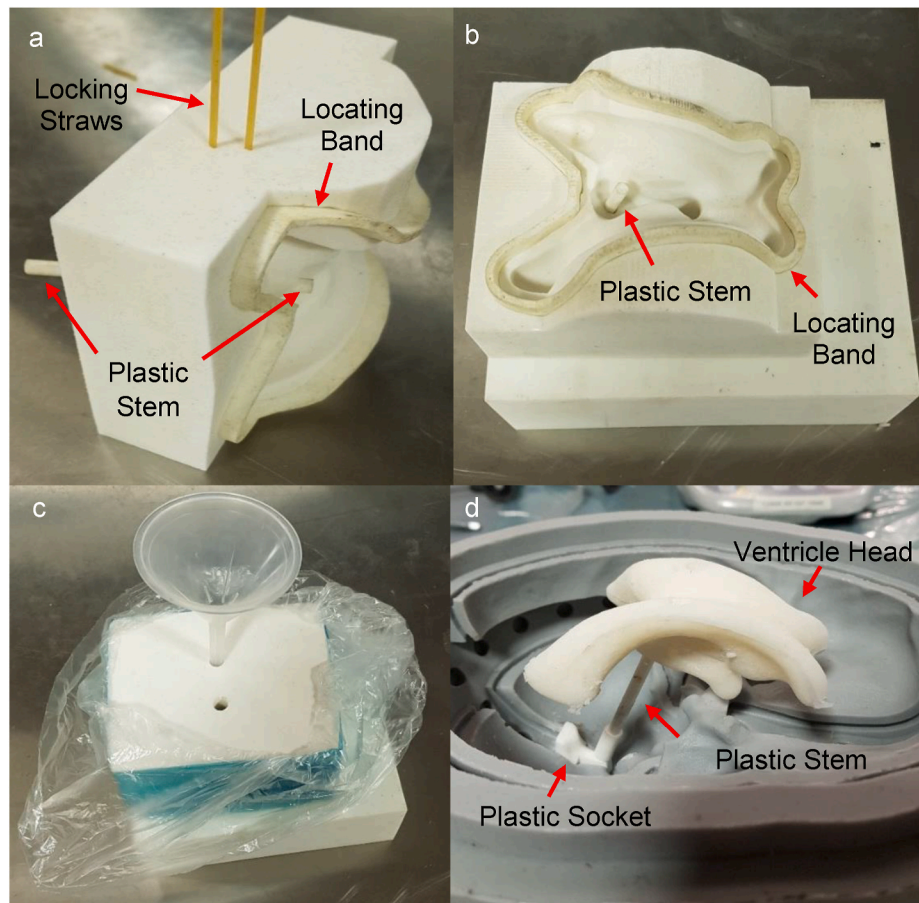
Fig. 4. Ice ventricle insert mould. a) bottom section of ventricle insert mould with DuraForm locating band and stem in place; b) top-down view of bottom section of ventricle insert mould; c) assembled mould on stand; d) ventricle cast in coconut oil for demonstration purposes and inserted into lower half of CBM.

be hinged away during insertion into the brain's fissures and then tied back together when in place (Fig. 7a and b).

A two-part skull was next designed and 3D printed in the DuraForm GF material (nominal tensile elastic modulus of approximately 4 GPa (DuraForm GF Plastic material data, 2017)), together with a silicone gasket (cast in the Mould Max 14NV material) to seal the skull on assembly. As shown in Fig. 7c and d, the two halves feature corresponding grooves to the dural septa's tabs which naturally co-locate when the brain-septa complex is placed in the lower skull half and the upper skull half is fastened on top via threaded nylon rods and nuts which occupy four tubes on the outside of each skull half. When fastened tightly together, the 5 mm thick gasket ensures that inside cavity is watertight.

Visible in Fig. 7e are also a set of features at the bottom of the skull for the fixation of the phantom to a mount system for MR and CT imaging (see later). Attached to the top of the skull are also six multi-modal fiducials (Beekley Medical, USA) to aid rigid registration of MR/CT images of the phantom (see Section 2.2.2.).

2.3.2. Phantom assembly

In order to prevent damage to the brain, phantoms were assembled in the same water-filled bucket used to thaw the brain. Here, the dural septa was first attached to the brain. The brain and dural septa were then drawn carefully into position in the lower skull half, where the tabs of the septa were pressed into their respective sockets. The threaded nylon rods were next pushed into the fastening tubes on the lower skull half and the silicone gasket was positioned over the lower skull half and nylon rods. The upper skull half was then lowered down onto the lower skull half with brain and dural septa in place, using the threaded rods as guides. The skull halves were then finally fastened together using the

nylon nuts, with the dural septa tabs naturally falling into position in the sockets of the upper skull half and a portion of the bucket's water intentionally being trapped within the skull to act as the CSF. This marked the completion of phantom assembly.

2.4. Phantom testing

It is well known that the mechanical properties of freeze-thaw PVA hydrogels are dependent on thawing rate and, since a substantially different thawing setup to Forte et al. was used in the brain fabrication workflow described above, it was identified that some tuning would be required to achieve a brain with realistic properties. In this work, the phantom's hydrogel brain was tuned along three dimensions: 1) its response to indentation, 2) its density differential with the CSF surrogate, and 3) the general magnitude of brain shift it produces in a phantom assembly.

As described in Section 2.2.1, the [3.00% PVA: 0.43% PHY: 96.57% Di H_2O] formula identified by Forte et al. was found to produce brains that were overtly too stiff (identified through palpation) when fabricated with the novel brain fabrication workflow presented in this work. Consequently, a series of brains with progressively lower PVA and PHY content were produced until a seemingly realistic brain (estimated initially through palpation) was reached.

An initial formula (IF) comprising [2.20% PVA: 0.26% PHY: 97.54% Di H_2O] was eventually found to produce a brain with seemingly realistic stiffness which was subsequently confirmed though indentation testing (see Appendix 2); however, the density of the material was found to be very close to that of the water CSF. Consequently, a modified version was formed which contained the additional component of granulated

Fig. 5. Demoulding of the CBM and transfer of the frozen brain to the thawing apparatus. a) bottom half of demoulded brain (frozen) showing exposed heads of map pins and fishing line bead anchors; b) top half of demoulded brain (frozen); c) frozen brain resting upside down in thawing cap with map pins and lines removed; d) frozen brain and thawing cap inside water bucket, placed inside incubator.
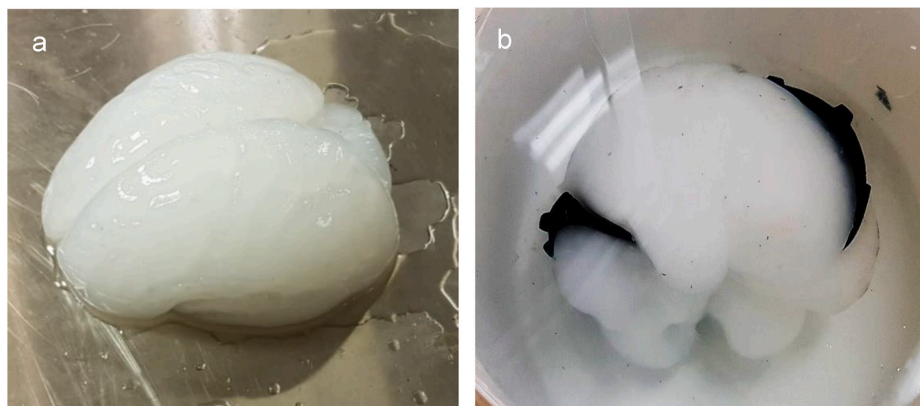

Fig. 6. *The fabricated brain.* a) fully thawed brain resting on a table, heavily deformed under its own weight; *b) fully thawed brain submerged in thawing bucket with dural septa part in fissures.*

white sugar (99% sucrose) mentioned in previous sections: [2.15% PVA: 0.25% PHY: 2.45% Sugar: 95.15% Di H_2O]. This formulation increased the hydrogel's density from 1.004 ± 0.003 to 1.010 ± 0.008 g/cm^3, doubling its submerged weight from approximately 9 to 18 g (see Appendix 1 for methods).

The following sections describe the methods that were used to assess the final two phantoms in the phantom's development. Phantom A represents the final iteration from which the SF was identified, while Phantom B represents the phantom which was used to conduct a full set of brain shift measurements. Although not explored fully in this work, the measurements from Phantom A were included to provide a sense of the repeatability of the phantom. Each phantom was first taken for PBS

simulation in a CT scanner and then subsequently taken for MR imaging to confirm construction. Following imaging, the brain was then harvested and mechanically tested through indentation. The time between defrosting the brain to indentation of the brain was kept under a week for all phantoms.

2.4.1. Brain shift imaging

To facilitate imaging in both MR and CT imaging environments, a multi-axis positioning cradle was fabricated for the phantom (Fig. 8). Although only supine to prone PBS is discussed in this work, the frame was developed with the capacity for further multi-position study (further details available in Appendix 1). The cradle was designed
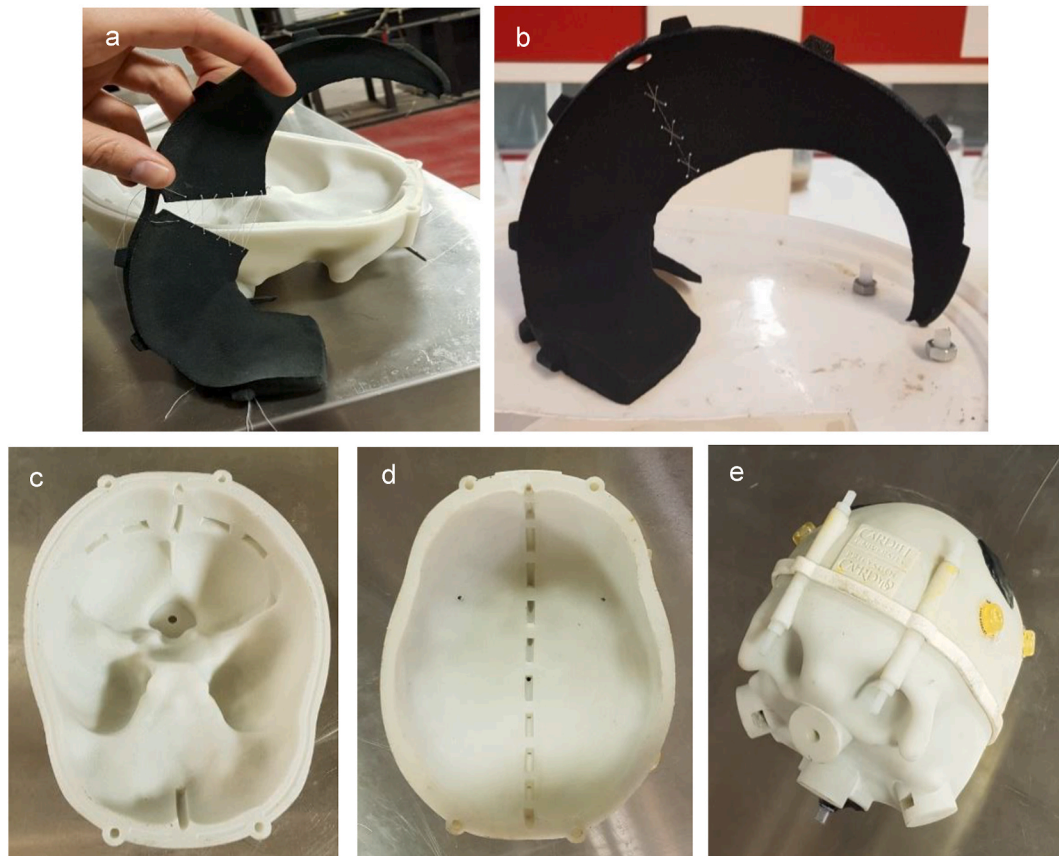
Fig. 7. Demonstration of dural septa part and skull system. a) dural septa part hinged away for delivery into brain's fissure spaces; b) dural septa part with line pulled taught and sections drawn together; c) lower skull half; d) upper skull half; e) assembled phantom with silicone gasket, nylon rods/nuts and imaging fiducials (yellow).

around a particular, cylindrical shaped, single channel head coil that was identified at the MR imaging suite utilised for this work: the Cardiff University Brain Research & Imaging Centre (CUBRIC), UK. The cradle was designed such that the phantom always rested in the centre of the head coil, at its isocentre.

Brain shift imaging, however, was conducted using CT imaging in order to avoid the significant image distortion present in MR images. A Revolution HD CT system based at Velindre Cancer Centre (UK) was used during the phantom's development to assess the brain shift produced by successive formulation iterations and, therefore, was the scanner used to image the brain shift in Phantom A. The CT element of a Discovery PET/CT 690 VCT system (GE Healthcare) based at the Wales Research and Diagnostic PET Imaging Centre (PETIC) (UK) was instead used to image Phantom B, due to the significantly longer scan time in taking repeat measurements. The former scanning system produced images with $0.63 \times 0.63 \times 0.63$ mm voxel dimensions, while the latter produced images with $0.45 \times 0.45 \times 0.63$ mm voxel dimensions.

To measure their PBS simulating capacity, Phantoms A and B were taken to the scanner, affixed to the cradle, and placed in the respective scanner's bore. Set in the supine position, the phantom was then allowed to settle for 3 min before being scanned. Following supine scanning, the phantom was then rotated around in the cradle and set in the prone position, where it was then allowed to rest for another 3 min, before being rescanned. Withphantom B, this process was repeated a further two times, obtaining three measurements in total (instead of single measurements for Phantom A).

Quantification of brain shift was performed by first rigidly registering the prone position scan to the supine position scan. This was done in 3D Slicer (Fedorov et al., 2012) using the BRAINSFit module (further information in Appendix 1). Brain shift was then quantified by

segmenting out the markers and measuring the per-marker displacement between the supine and prone images.

In addition to brain shift imaging, three successive supine scans were also taken of phantom B prior to brain shift imaging to examine the repeatability of the marker centroid determination process. Here, the second and third supine scans were both registered to the initial scan and the displacement between the marker centroids was extracted.

2.4.2. Construction confirmation

Phantoms A and B were all imaged with MRI following CT brain shift imaging to confirm that the phantom was constructed properly. This was performed at CUBRIC using a 3 T Prisma system, the aforementioned head coil and a T2-weighted, 2D turbo spin echo sequence. This setup produced high contrast scans (allowing for easy part boundary identification) with 0.43×0.43 mm in-plane voxel dimensions and a 2D slice thickness of 3.25 mm. Each phantom was placed in the cradle, locked in the supine position, and allowed to rest for 3 min before commencing the scan.

2.4.3. Indentation testing

Following imaging, the brains of Phantoms A and B were retrieved and subjected to indentation testing. For each brain, the left and right hemispheres were isolated and two flat segments were harvested from each (four in total). For each set of hemisphere segments, indentation was then performed at nine locations across three of the available surfaces (see Appendix 1) (18 tests in total). Since the hydrogel was found to produce very porous brain gels which expel a significant proportion of their water content under their own weight, the segments were indented underwater in a bucket of room temperature deionised water.

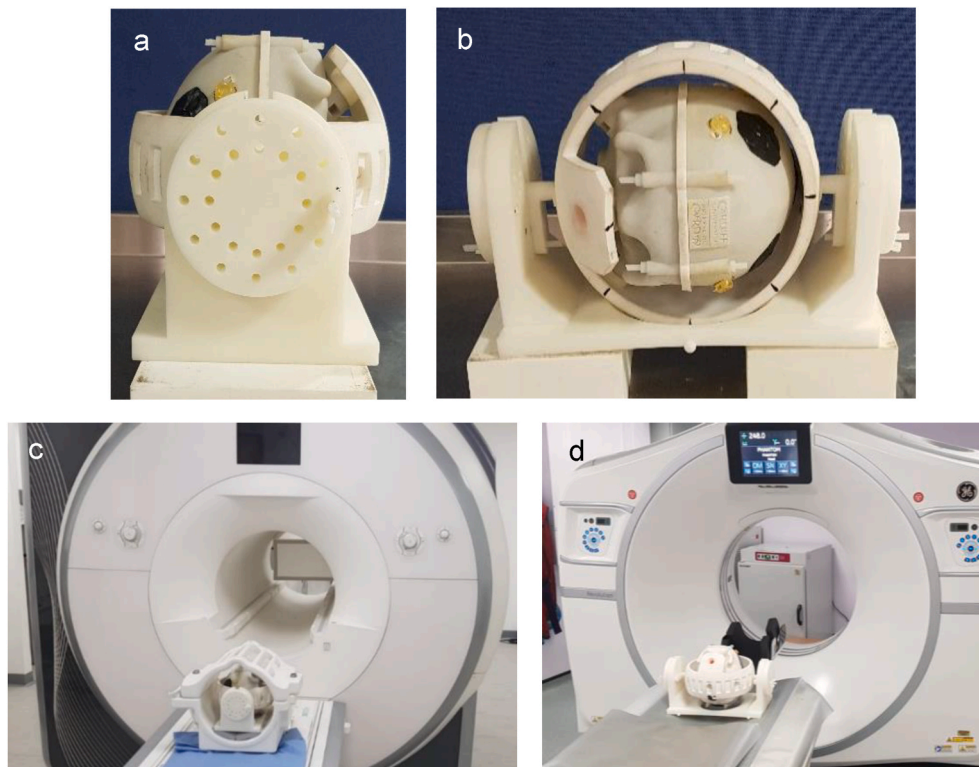For each indentation test, a 6 mm diameter spherical ruby indenter

Fig. 8. Brain shift imaging with the phantom cradle. a) phantom orientated in supine position in cradle; b) phantom orientated in left decubitus position in cradle; c) phantom loaded into single channel head coil in mock MR scanner; d) phantom prepared for CT scanning.

was driven down towards the cerebral segment until a touching load was found. At this point the indenter was then driven down 6 mm at a rate of 1 mm/s and held at 6 mm depth for 500 s. Due to the delicacy of the setup, a touching load was found difficult to identify, especially with the 10 N load cell available (accurate to ±1% at 0.1 N). Here, the most consistent approach in identifying a touching load was found empirically to be in manually lowering the indenter at a rate of approximately 0.08 mm/s until a consistent climb towards 3 μN was observed. At 3 μN the test was then manually triggered. This approach produced acceptable curves with minimal inconsistencies at the start.

This indentation protocol is the same as used by Leibinger et al. (2016), who performed indentation measurements on both the CH and porcine brain tissue. The use of the same protocol, therefore, provided a direct means of comparison. To further compare to the wider results in the literature concerning the more general stiffness of brain tissue, an approximate elastic modulus range was obtained from the phantom brain indentations. This was calculated using the indentation force-displacement to elastic modulus conversion equation developed by Czerner et al. (2015). Rearranged from the way it was presented by Czerner et al., this equation is shown in Equation 2.1, where E is the elastic modulus, r is the radius of the indenter, h is the height (depth/displacement) of the indenter and P is the force measured at the depth.

$$E\ (Pa) = \frac{9(P)}{16\left(r^{\frac{1}{2}}\ h^{\frac{3}{2}}\right)}$$

For each brain, an elastic modulus range was estimated by entering in the force and displacement measured at 4 mm depth for the steepest and flattest curve. Further statistical assessment of the data was not performed due to the uncertainty in measuring indenter depth with respect to the surface of the hydrogel samples. Given the wide range of values reported for brain tissue, a stiffness in the general range was considered sufficient, provided similar force-displacement and relaxation curve shapes were obtained from the material.

3. Results

3.1. Mechanical testing

Presented in Fig. 9 are representative loading curves for the SF hydrogel material from phantom B, and the comparative data from Leibinger et al. (2016). Aside from the atypical toe regions of the loading curve (see below), it can be seen that the variability is acceptably small for the SF hydrogel material that it produces similarly shaped loading and relaxation curves to those measured by Leibinger et al. for porcine brain tissue and the CH. However, peak loads at 6 mm depth of approximately 0.02–0.04 N were measured for the SF material, which are somewhat lower than the approximate peak loads of 0.1 and 0.13 N measured by Leibinger et al. for porcine brain tissue and the CH, respectively. Yet, approximate elastic modulus ranges of 0.65–0.86 and 0.50–1.06 kPa were measured for phantoms A and B, respectively, which lie well within the 0.3–3.0 kPa stiffness range that can be seen in the wider literature for brain tissue across multiple species (Budday et al., 2015; Christ et al., 2010, van Dommelen et al., 2010; Kaster et al., 2011).

The atypical toe regions of the SF loading curves were unfortunately a result of the aquatic testing environment required to mechanically test the cerebral segments. Here, the acceleration of the indenter at the start of each test generated an oscillatory output from the load cell which, when averaged, produced the toe regions visible in the graphs of Fig. 9. It should be noted that, for both of the datasets presented, the curves can be seen to stabilize by 1 mm displacement.

3.2. Imaging of phantom construction

MR imaging of Phantoms A and B revealed each to contain a reasonable reconstruction of the anatomical system. Realistic compartmentation of the cranial cavity was achieved by the dural septa and a reasonable recreation of the SAS, ventricles and fissures can be seen. A
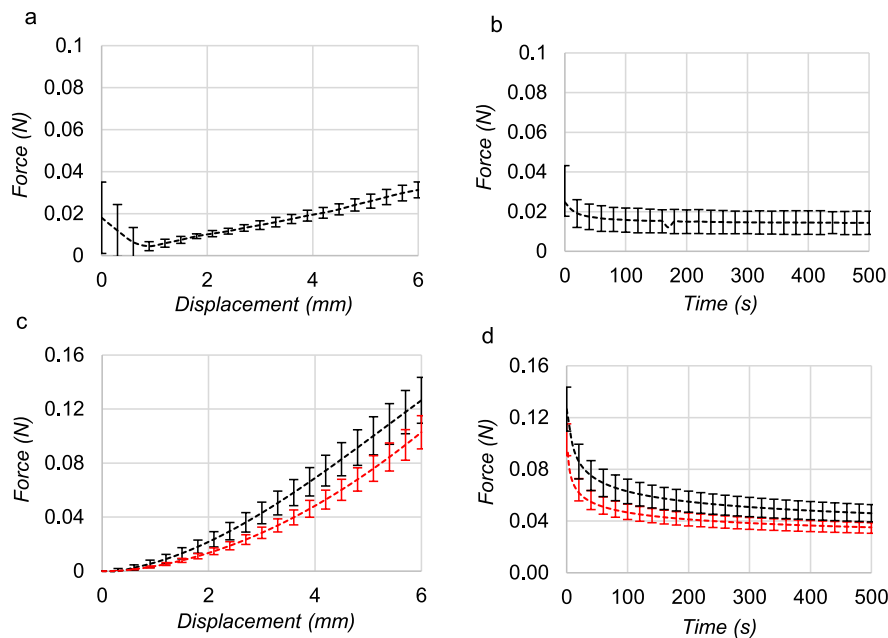
Fig. 9. Representative loading and relaxation curves obtained from indenting the SF hydrogel, together with re-plotted loading and relaxation data from Leibinger et al. (2016) for brain and CH. [a] and [b] are the loading data and relaxation data, respectively, obtained from phantom B; [c] and [d] are the re-plotted loading and relaxation data, respectively, for brain (red line) and CH (black line), originally presented by Leibinger et al. (2016).

representative collection of cross-sectional MR images (and two example CT images) of Phantom B are shown in Fig. 10.

Yet, while largely formed as intended, minor construction errors were discovered in the two phantoms. In Phantom A it was found that the left cerebellum had been caught between the dural septa and the skull on assembly, while in Phantom B, a 4 ml volume of air had become trapped. A much smaller collection of trapped air was found in Phantom A (1.7 ml).

3.3. Brain shift simulation

Average (mean ± standard deviation) supine to prone brain shifts of 1.03 ± 0.37 and 0.93 ± 0.28 mm were measured in phantoms A and B (average of repeats in the case of phantom B), respectively. This is in combination with ranges of 0.08–1.66 and 0.48–1.52 mm, respectively. For phantom B, average brain shifts of 1.03 ± 0.39, 0.90 ± 0.38 and 0.90 ± 0.31 mm were measured for the three individual measurements, respectively. This is in combination with ranges of 0.11–1.74, 0.09–1.62 and 0.19–1.50 mm, respectively. Average marker displacement between the repeat supine scans of phantom B was measured to be 0.06 ± 0.03 and 0.05 ± 0.02 mm between the first and second and the first and third scans, respectively, indicating high repeatability in the imaging and brain shift extraction process.

Presented in Fig. 11 are axial and sagittal views of the vector fields (exaggerated in magnitude by a factor of 8) measured in phantoms A and B. Here, it can be seen that a clear non-rigid shifting of the brain takes place within these phantoms.

A small asymmetry in shift magnitude was measured in phantom B which was not measured in phantom A. In phantom B, average brain shift was measured to be 1.10 ± 0.22 and 0.77 ± 0.23 mm for the left and right side, respectively, while for phantom A, average brain shift was measured to be 1.03 ± 0.44 and 1.02 ± 0.29 mm for the left and right side, respectively.

4. Discussion

The phantom presented in this work represents the first attempt

made towards creating a full brain-skull model for the purpose of PBS simulation. At the time of writing, the CUBS phantom is the first to combine a biofidelic (geometrically and mechanically realistic) brain with fluid-filled ventricles, biofidelic dural septa, biofidelic fluid-filled SAS and biofidelic cranial cavity. This was made possible by the development of an entirely novel set of moulds (composite brain mould and ventricle mould), parts (dural septa, two-part skull and thawing apparatus) and fabrication/assembly workflows.

Critical to the development of the phantom was the utilization of the intermediate frozen curing state of the CH material developed by Forte et al. (2016). This unique feature allows for the moulding and retrieval of complex shapes that would otherwise be impossible to achieve with other established brain material surrogates (due to their inherent fragility). Using the composite brain mould, ice ventricle mould and thawing apparatus, a workflow was established for the moulding of a full brain geometry in the validated CH material.

Brains produced with this workflow can be seen in the MR images of Fig. 10 to comprise cerebrum, cerebellum and brain stem, with realistic partitioning by the medial longitudinal fissure and transverse cerebral fissure, and inclusion of an approximation of the internal ventricle cavity. Although sulci depth was significantly reduced for application in the PBS simulation case, it should be noted that this feature could also be recreated with only small changes to the mould design.

In addition to geometry, the indentation measurements of phantoms A and B show that brains fabricated with the workflow and the CH material contain mechanical properties that are consistent with that measured for brain tissue in the literature. Brains produced with the SF have general stiffnesses that are well within the 0.3–3.0 kPa range measured for brain tissue (Budday et al., 2015; Christ et al., 2010) and the loading and relaxation curve shapes are similarly consistent. The two brains produced with the SF, for example, were measured to have stiffness ranges of 0.65–0.86 and 0.50–1.06 kPa, respectively. Although inter-phantom variability was not rigorously investigated in this work, an encouragingly small variation can be seen between the stiffness ranges of brains that were made with the SF.

Through the intentional use of similar methods (same indenter dimensions and displacement profile), direct comparison was made
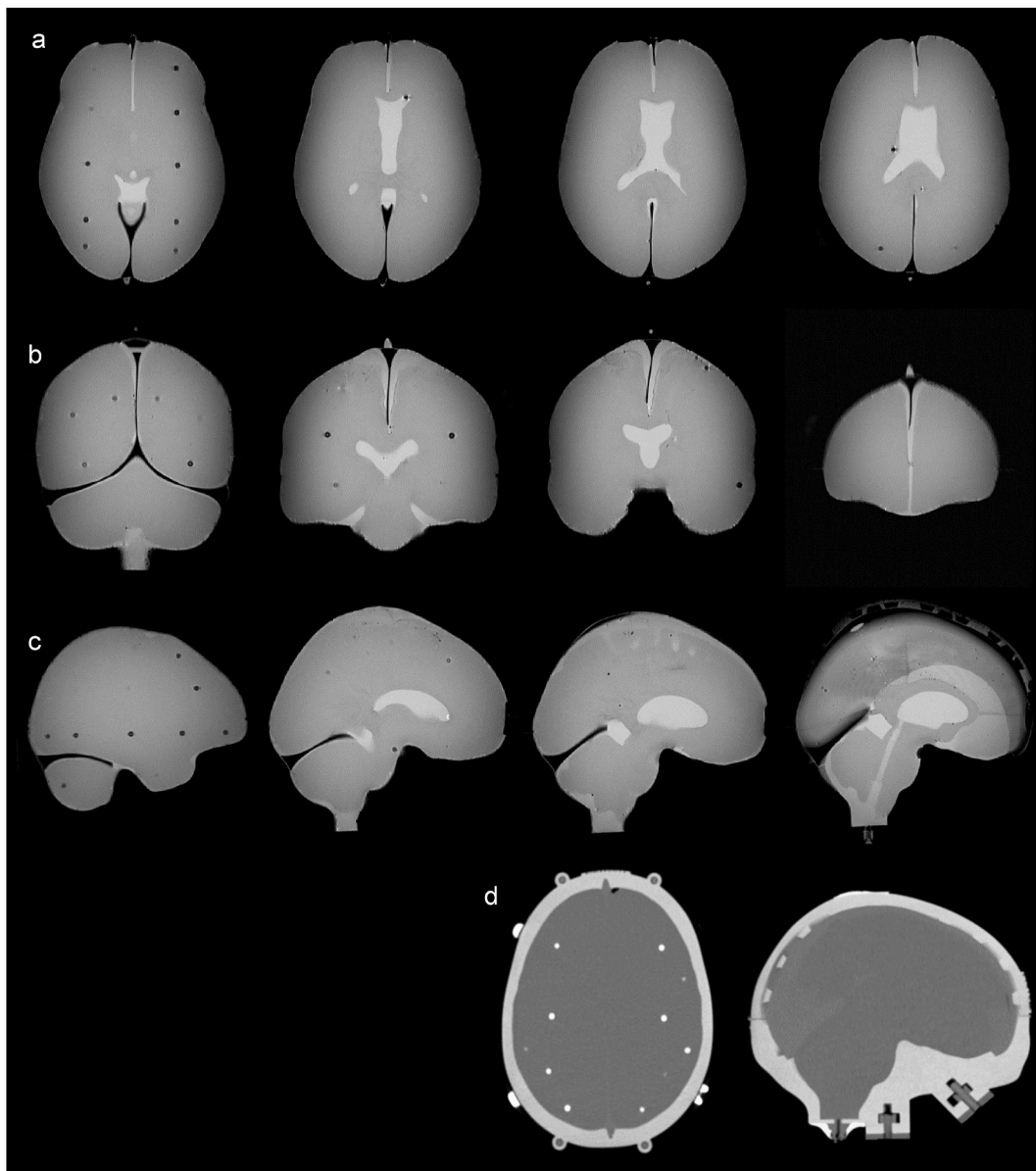
Fig. 10. Cross-sectional MR and CT images of phantom B. Row [a] shows a selection of axial MR images in order of inferior to superior. Row [b] shows a selection of coronal MR images in order of posterior to anterior. Row [c] show a selection of sagittal MR images in order of the left to the centre. Row [d] contains one axial and one sagittal CT image.

available to the porcine brain and CH material indentation measurements by Leibinger et al. (2016). In their work, Leibinger et al. demonstrated the CH to produce similarly shaped loading and relaxation curves to porcine brain tissue, with similar peak loads of 0.13 and 0.10 N measured for porcine brain and CH, respectively. While peak loads can be seen in Fig. 9 to be considerably lower for the SF (~0.02–0.04 N range) version of the CH, the shapes of the loading and relaxation curves can be considered to be more or less the same. Both versions of the CH material can be seen to produce an upward curve during the initial 6 mm insertion of the indenter, which is followed by a rapid relaxation of the material when the indenter is held, dropping to give approximately half the load after 200 s.

Despite the addition of sugar to increase the mass of the hydrogel, the density of the SF (1.0004 ± 0.008 g/cm^3), however, could only be pushed so far towards the 1.030–1.050 g/cm^3 literature range for brain tissue (Barber et al., 1970; DiResta et al., 1990; Faas and Ommaya, 1968; Rouessle and Roulet, 1932; Sankey, 1853), resulting in a much lower submerged weight of 18 g in the phantom when compared to the

40–100 g submerged weight of the anatomical brain (see Appendix 1 for calculation method). This was because the sugar also had a plasticizing effect and so further addition also reduced its stiffness. Yet, despite this, the SF brain's stiffness and submerged weight was found to produce comparable brain shift magnitudes to that measured in humans with MRI for the supine to prone transition, with average magnitudes of 1.03 ± 0.37 and 0.93 ± 0.28 mm measured in Phantoms A and B, respectively. Mikkonen and Laakso (2019), for example, measured average cortical shifts of 0.8 ± 1.1 and 0.7 ± 1.0 mm for the right and left hemispheres, respectively, while Schnaudigel et al. (2010) reported a range of 0.6–1.3 mm, presenting most of the brain shift measured instead in vector graphic format. These values are further supported by observations of "up to 1 mm" and "approximately 1 mm" by Hill et al. (1998) and Rice et al. (2013), respectively, in studies less focused on PBS. A third major study on PBS by Monea et al. (2012) reported brain shift as cortical and ventricular normal-to-surface displacement (positive values = outward displacement), with values of 0.47 ± 1.90 and 0.06 ± 0.63 mm reported for cortical and ventricular brain shift in the
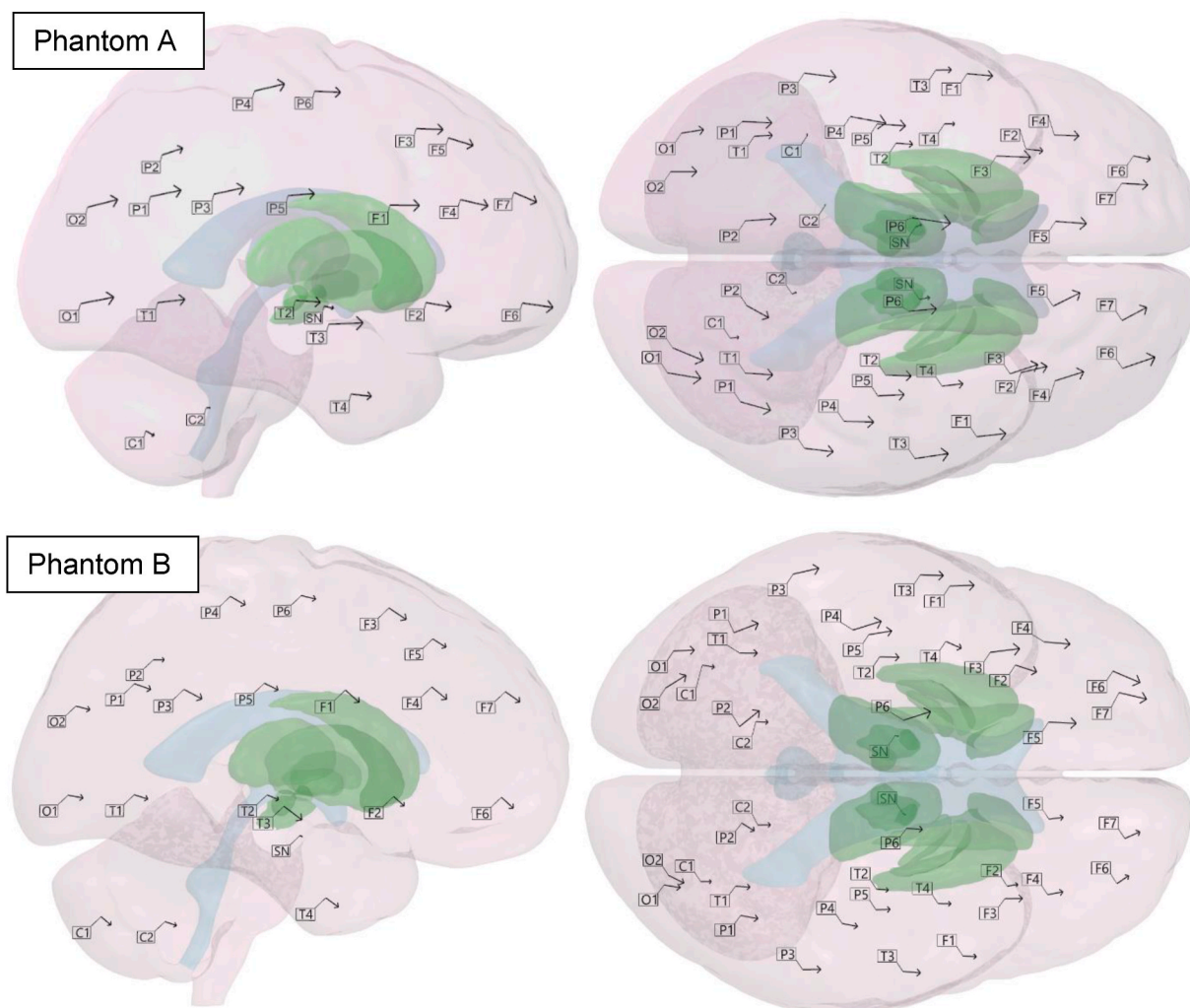
Fig. 11. Sagittal and axial brain shift maps obtained from phantoms A and B, with vector magnitude exaggerated by a factor of 8 for visibility. Vector fields are displayed together with the segmented MNI brain model which was spatially aligned with each 3D vector field by rigidly registering the MNI dataset with the supine image of each phantom and applying the same transform to the extracted 3D brain model. Vector labels correspond roughly to the region of the brain the markers are located in with C, O, T, P and F referring to the cerebellar, occipital, temporal, parietal and frontal regions, respectively. The sub-nuclear marker, SN, marker sits beneath the Substania Nigra.

25–40 age bracket, respectively (data for two other age brackets are also presented). Most recently, Zappala et al. (Zappalá et al., 2021) measured a mean displacement of 0.57 ± 0.34 mm in a young cohort (age range of 22–32 years), with significant displacements ranging from 0.52 to 0.77 mm at surgically relevant structures (e.g. the subthalamic nucleus).

Similar measurements were obtained for the three individual measurements of phantom B with individual average shifts of 1.03 ± 0.39, 0.90 ± 0.38 and 0.90 ± 0.31 mm and individual ranges of 0.11–1.74, 0.09–1.62 and 0.19–1.50 mm measured, indicating good intra-phantom repeatability and reliability in the brain shift imaging/quantification process. Importantly, these values are very similar to the aforementioned literature measurements of supine to prone brain shift. Furthermore, as can be seen in the sagittal and axial vector graphics of the two SF phantoms (A and B) (Fig. 11), the shift which manifests is clearly nonrigid, with both variable magnitude and direction of shift present.

Unlike phantom A, however, which contained only 1.7 ml air, phantom B featured an accidental inclusion of 4.0 ml of air. This air volume largely resided on the left side of the cranial cavity (partitioned by the dural septa), shifting consistently between the frontal and occipital regions on transition from supine to prone. As can be seen in the vector graphics, a left-right asymmetry in shift can also be seen, with the left side undergoing greater shift than the right side. This enhancement

of shift with intracranial air is consistent with observations in patients where similar unilateral air invasion has occurred as a result of CSF loss during surgery. Miyagi et al. (2007), for example, observed a combination of downward shift beneath the air collection and lateral shift towards the contralateral side of the cranial cavity upon unilateral invasion of air. Such pneumocephalus air volumes, however, are typically far greater than 4 ml and, unlike in the anatomy, the air volume in the phantom moves through the SAS, likely enhancing gravitational sag in opposing directions with positional transition. Air effects in the phantom, therefore, require further study to understand. It is also possible that some of the asymmetry could be due to subtle differences in brain geometry arising from the manufacturing process or trapping of the brain against the tight-fitting skull on assembly. Repeat experimentation with further phantoms would help understanding here.

The influence of such small air volumes presents a problem in phantom fabrication, as very small volumes are difficult to eliminate during assembly. Despite a very careful approach involving full assembly underwater, air volumes were always found in imaged phantoms and with varying distribution. In some cases, the majority of the air was present in the ventricle, while in others the majority of the air would be held in one of the left or right cranial compartments partitioned by the dural septa. Post-assembly air removal ports were trialled with the

phantom, however, these were not found to be helpful as suction appeared to be inhibited by the complex compartmentalisation and narrow nature of the SAS. The dural septa, therefore, provides part of the problem, however, this feature is a key part of the anatomy and it is unlikely that such a realistic shift would have been captured in the phantom without it. Chen et al. (2011), for example, found an increase in subsurface brain shift prediction accuracy when including the dural septa in modelling. However, the effect of the feature in the phantom should be determined through repeat measurements in phantoms with and without the part.

Regardless of any slight shift asymmetry induced by the inclusion of air, the developed phantom has been shown to be capable of realistically recreating the magnitude and non-rigid nature of the supine to prone positional brain shift event. At this level of validation, the phantom should be able to be used to develop insights into the shift that occurs within other surgical positional transitions. Furthermore, at this level of validation, the phantom could also be potentially used as a neurosurgical training tool, providing a risk-free training case for surgeons looking to gain an understanding of what shift might occur in a real-life patient. It also has potential to be used to test other procedures such as drug delivery or electrode placement, since the hydrogel has similar toughness and subjective cutting properties to real brain tissue (Forte et al., 2016). Further validation is required, however, in order to use the phantom's brain shift maps in any sort of correctional software for neurosurgical planning. For this to occur, the phantom's brain shift maps would need to be validated against similarly comprehensive maps obtained from humans with MR or CT imaging. As yet, such data is not available.

5. Limitations

The foremost limitation of this study was the 4 ml volume of air that was incorporated into phantom B during assembly. As discussed, such small air volumes are difficult to eliminate and are only visible at the end of the fabrication and experimental process (post-processing of scans into 3D models). Air removal systems were trialled with the phantom during its development, but they were found to be ineffective and increased the risk of leakage.

The second principal limitation is in the lack of repeat measurements in further additional phantoms, which would have been helpful in answering some of the questions highlighted by the presented work. This was made difficult by the long and problematic development profile for the phantom, made so by a) the week long cycle time for the fabrication, MR/CT imaging and mechanical testing of each iteration of the phantom, b) the loss of time due to fabrication failures and, c) the accruement of cost at each scanning stage.

The third principal limitation pertains to the resolution of the CT scanners employed which, with voxel resolutions of $0.45 \times 0.45 \times 0.63$ and $0.63 \times 0.63 \times 0.63$ mm^3 for the Revolution Discovery systems, respectively, could be considered ill-suited to measure displacements ranging 0–2 mm. However, with displacements less than 0.1 mm being measured between repeat scans of the phantom, the Discovery PET/CT system was found to be reliable. Although this same assessment was not performed for Revolution system, a similar degree of repeatability would likely have been found. Unlike the Discovery system, the Revolution system was available for use daily, but could only be used for short periods during breaks in clinical scanning, therefore only short experiments could be conducted on a charitable basis. However, use of this scanner was invaluable in the trial and error process involved in identifying a viable phantom.

The fourth principal limitation concerns the fidelity of the phantom which, while containing a novel broad set of features, did not contain a full recreation of the feature set which mechanically defines the brain-skull system. While the fluid-filled space aspect of the SAS was recreated, the solid fraction (e.g. arachnoid trabeculae, blood vessels, etc.) is absent. These elements act to tether the pia to the arachnoid, and

therefore the brain to the skull, and so likely play a role in PBS. However, the extent to which the solid fraction affects PBS is not clear, since the mechanical properties of the SAS are both difficult to measure and difficult to then implement (and vary) in either phantom or computational models. Recreating the solid fraction was investigated, but no means could be found to fabricate such a complex interface with the appropriate mechanical properties (see Potts, 2020). In addition to the simplifications of the SAS, the brain was also represented by a single material, with no differentiation between white and grey matter. However, there is little evidence of differing properties at low strain rates (Potts, 2020) and, therefore, this simplification likely had a minimal effect in simulating PBS. Lastly, there is also the question of to what degree the poroelasticity of the brain was reproduced in the phantom. However, given the small strains involved in PBS, the brain shift resulting from fluid flow is likely to minimal. This is supported by the fact that Bennion et al. (2022) was able to reproduce PBS in a computational model using a purely hyperelastic material model with no capacity for fluid flow.

6. Conclusions

This work demonstrates that superior phantoms can be produced through production workflows that utilize the frozen intermediate stage of freeze-thaw brain material surrogates. Using this feature, a phantom was able to be built which contained full brain with fluid-filled ventricle/fissure spaces, fluid-filled SAS, dural septa and skull, all with realistic geometry and mechanical properties. This comprehensive recreation of the brain-skull system in-turn provided the capacity for realistic brain shift simulation, allowing comparable magnitude and non-rigid brain shift pattern to manifest in the phantom on repositioning from the supine to the prone head position.

At its current level of validation, the phantom should be capable of providing insights into the shift that occurs within other surgical positional transitions, providing similarly novel pictures of the shift to the picture produced in this work for the supine to prone event. This information is difficult to produce through *in vivo* measurement, due to the limited way in which patients can be placed in MRI scanners (e.g. due to head coil shape) and the compounding scanning time for each position investigated (accruing cost and comfort issues), and should help surgeons better understand the brain shift that is likely to occur during any given surgery, leading to lower targeting error and better clinical outcomes.

While some time and cost is required in preparing the moulds and parts of the fabrication workflow, the necessary laboratory equipment is common and the brain itself is cheap to make once the workflow is established. If the phantom were to be validated further, with respect to surgical implement resistance, for example, it could therefore be potentially used as a neurosurgical training tool. This would provide trainee surgeons with a risk-free simulator that they can use freely to hone their techniques.

CRediT authorship contribution statement

Matthew R. Potts: Writing – review & editing, Writing – original draft, Validation, Methodology, Investigation, Formal analysis, Conceptualization. **Nicholas J. Bennion:** Writing – review & editing, Methodology, Conceptualization. **Stefano Zappalá:** Writing – review & editing, Methodology, Conceptualization. **David Marshall:** Writing – review & editing, Supervision, Methodology, Conceptualization. **Rob Harrison:** Supervision, Resources, Funding acquisition. **Sam L. Evans:** Writing – review & editing, Supervision, Methodology, Funding acquisition, Conceptualization.

Declaration of competing interest

The authors declare the following financial interests/personal

relationships which may be considered as potential competing interests: Matthew Potts reports financial support was provided by EPRSC. Matthew Potts reports financial support was provided by Renishaw Plc.

Data availability

Data will be made available on request.

Acknowledgments

The authors would like to thank Allison Cooper, Peter Hobden and the wider CUBRIC team for their assistance in the MR imaging of the phantom. Similarly, the authors would also like to thank Gill Gaywood and the wider radiology team at Velindre Cancer Centre, and Rhodri Smith and the wider radiology team at PETIC for their assistance in CT scanning the phantom.

This research was funded by the EPSRC, Renishaw plc and Cardiff University.

Appendix A. Supplementary data

Supplementary data to this article can be found online at https://doi.org/10.1016/j.jmbbm.2023.105704.

References

Barber, T.W., Brockway, J.A., Higgins, L.S., 1970. The density of tissues in and about the head. Acta Neurol. Scand. 46, 86–92.

Bayer, S., Wydra, A., Zhong, X., Ravikumar, N., Strumia, M., Schaffert, R., Ostermeier, M., Fahrig, R., Maier, A., 2018. An Anthropomorphic Deformable Phantom for Brain Shift Simulation. In: 2018 IEEE NSS/MIC Conference Record.

Bennion, N.J., Zappalá, S., Potts, M., Wooley, M., Marshall, D., Evans, S.L., 2022. In Vivo Measurement of Human Brain Material Properties under Quasi-Static Loading. J R Soc Interface, 20220557. https://doi.org/10.1098/rsif_2022_0557 (in press).

Bilger, A., Dequidt, J., Duriez, C., Cotin, S., 2011. Biomechanical simulation of electrode migration for deep brain stimulation. Lect. Notes Comput. Sci. 339–346.

Budday, S., Nay, R., de Rooij, R., Steinmann, P., Wyrobek, T., Ovaert, T.C., Kuhl, E., 2015. Mechanical properties of gray and white matter brain tissue by indentation. J. Mech. Behav. Biomed. Mater. 46, 318–330.

Chen, S.J., Hellier, P., Gauvrit, J.Y., Marchal, M., Morandi, X., Collins, D.L., 2010. An anthropomorphic polyvinyl alcohol triple-modality brain phantom based on Colin27. Med. Image Comput Comput. Assist Interv. 13 (2), 92–100.

Chen, I., Coffey, A.M., Ding, S., Dumpuri, P., Dawant, B.M., Thompson, R.C., Miga, M.I., 2011. Intraoperative brain shift compensation: accounting for dural septa. IEEE Trans. Biomed. Eng. 58 (3), 499–508.

Chen, I., Ong, R.E., Simpson, A.L., Sun, K., Thompson, R.C., Miga, M.I., 2013. Integrating retraction modelling into an atlas-based framework for brain shift prediction. IEEE Trans. Biomed. Eng. 60 (12), 3494–3504.

Christ, A.F., Franze, K., Gautier, H., Moshayedi, P., Fawcett, J., Franklin, R.J., Karadottir, R.T., Guck, J., 2010. Mechanical difference between white and gray matter in the rat cerebellum measured by scanning force microscopy. J. Biomech. 43 (15), 2986–2992.

Clatz, O., Delingette, H., Bardinet, E., Dormont, D., Ayache, N., 2003. Patient-specific biomechanical model of the brain: application to Parkinson's disease procedure. Surgery Simulation and Soft Tissue Modeling 321–331.

Czerner, M., Fellay, L., Suárez, M., Frontini, P., Fasce, L., 2015. Determination of elastic modulus of gelatin gels by indentation experiments. Procedia Materials Science 8, 287–296.

DeLorenzo, C., Papademetris, X., Vives, K.P., Spencer, D.D., Duncan, J.S., 2007. A comprehensive system for intraoperative 3D brain deformation recovery. Med. Image Comput Comput. Assist Interv. 10 (2), 553–561.

DiResta, G.R., Lee, J., Lau, N., Ali, F., Galicich, J.H., Arbit, E., 1990. Measurement of brain tissue density using pycnometry. Acta Neurochir. Suppl. 51, 34–36.

DuraForm Flex material data sheet [Internet]. 3D Systems. [updated 2020; cited 18/03/2021]. Available from: https://uk.3dsystems.com/sites/default/files/2020-09/3d-systems-duraform-flex-sls-datasheet-usen-2020-09-21-a-print.pdf.

DuraForm GF Plastic material data sheet [Internet]. 3D Systems. [updated 2017; cited 18/03/2021]. Available from: https://uk.3dsystems.com/sites/default/files/2017-06/3D-Systems_DuraForm_GF_DATASHEET_USEN_2017.06.08_WEB.pdf.

Faas, F.H., Ommaya, A.K., 1968. Brain tissue electrolytes and water content in experimental concussion in the monkey. J. Neurosurg. 28 (2), 137–144.

Fedorov, A., Beichel, R., Kalpathy-Cramer, J., Finet, J., Fillion-Robin, J.-C., Pujol, S., Bauer, C., Jennings, D., Fennessy, F.M., Sonka, M., Buatti, J., Aylward, S.R., Miller, J.V., Pieper, S., Kikinis, R., 2012. 3D slicer as an image computing platform for the quantitative imaging network. Magn. Reson. Imag. 30 (9), 1323–1341.

Forte, A.E., Galvan, S., Manieri, F., Rodriguez, y, Baena, F., Dini, D., 2016. A composite hydrogel for brain tissue phantoms. Mater. Des. 112, 227–238.

Forte, A.E., Galvan, S., Dini, D., 2018. Models and tissue mimics for brain shift simulations. Biomech. Model. Mechanobiol. 17 (1), 249–261.

Hill, D.L.G., Maurer, C.R., Maciunas, R.J., Barwise, J.A., Fitzpatrick, J.M., Wang, M.Y., 1998. Measurement of intraoperative brain surface deformation under a craniotomy. Neurosurgery 43 (3), 514–526.

Hu, J., Jin, X., Lee, J., Zhang, L., Chaudhary, V., Guthikonda, M., et al., 2007. Intraoperative brain shift prediction using a 3D inhomogeneous patient-specific finite element model. J. Neurosurg. 106 (1), 164–169.

ICBM 152 Nonlinear atlases version, 2009. The McConnell brain imaging centre [Internet], [updated 2014; cited 17/06/2018]. Available from: http://www.bic.mni.mcgill.ca/ServicesAtlases/ICBM152NLin2009.

Ji, S., Margulies, S.S., 2007. In vivo pons motion within the skull. J. Biomech. 40 (1), 92–99.

Ji, S., Zhu, Q., Dougherty, L., Margulies, S.S., 2004. In vivo measurements of human brain displacement. Stapp Car Crash J 48, 227–237.

Kaster, T., Sack, I., Samani, A., 2011. Measurement of the hyperelastic properties of ex vivo brain tissue slices. J. Biomech. 44 (6), 1158–1163.

Leibinger, A., Forte, A.E., Tan, Z., Oldfield, M.J., Beyrau, F., Dini, D., Rodriguez Y Baena, F., 2016. Soft tissue phantoms for realistic needle insertion: a comparative study. Ann. Biomed. Eng. 44 (8), 2442–2452.

Ma, J., Wittek, A., Singh, S., Joldes, G., Washio, T., Chinzei, K., Miller, K., 2010. Evaluation of accuracy of non-linear finite element computations for surgical simulation: study using brain phantom. Comput. Methods Biomech. Biomed. Eng. 13 (6), 783–794.

Mikkonen, M., Laakso, I., 2019. Effects of posture on electric fields of non-invasive brain stimulation. Phys. Med. Biol. 64 (6), 065019.

Miyagi, Y., Shima, F., Sasaki, T., 2007. Brain shift: an error factor during implantation of deep brain stimulation electrodes. J. Neurosurg. 107 (5), 989–997.

Mohammadi, A., Ahmadian, A., Azar, A.D., Sheykh, A.D., Amiri, F., Alirezaie, J., 2015. Estimation of intraoperative brain shift by combination of stereovision and Doppler ultrasound: phantom and animal model study. Int. J. Comput. Assist. Radiol. Surg. 10 (11), 1753–1764.

Monea, A.G., Verpoest, I., Vander Sloten, J., Van der Perre, G., Goffin, J., Depreitere, B., 2012. Assessment of relative brain-skull motion in quasistatic circumstances by magnetic resonance imaging. J. Neurotrauma 29 (13), 2305–2317.

Navarro-Lozoya, M., Kennedy, M., Dean, D., Rodriguez-Devora, J., 2019. Development of phantom material that resembles compression properties of human brain tissue for training models. Materialia 8, 100438.

Potts, M., 2020. A Phantom for Positional Brain Shift [dissertation]. Cardiff University.

Puzrin, A., Skrinjarb, O., Ozanc, C., Kimc, S., Mukund, S., 2005. Image guided constitutive modelling of the silicone brain phantom. SPIEL 5744, 157–164.

Reinertsen, I., Collins, D.L., 2006. A realistic phantom for brain-shift simulations. Med. Phys. 33 (9), 3234–3240.

Rice, J.K., Rorden, C., Little, J.S., Parra, L.C., 2013. Subject position affects EEG magnitudes. Neuroimage 64, 476–484.

Rouessle, R., Roulet, F., 1932. Mass und Zahl in der Pathologie. Pathologie und Klinik in Einzeldarstellungen. Verlag yon Julius Springer, Berlin und Wien, p. 87.

Sankey, W.H.O., 1853. The specific gravity of the brain. Brit. Med. Chir. Rev. 240–257.

Schnaudigel, S., Preul, C., Ugur, T., Mentzel, H.J., Witte, O.W., Tittgemeyer, M., Hagemann, G., 2010. Positional brain deformation visualized with magnetic resonance morphometry. Neurosurgery 66 (2), 376–384.

Skrinjar, O., Nabavi, A., Duncan, J., 2002. Model-driven brain shift compensation. Med. Image Anal. 6 (4), 361–373.

Sun, K., Pheiffer, T., Simpson, A., Weis, J., Thompson, R., Miga, M., 2014. Near real-time computer assisted surgery for brain shift correction using biomechanical models. IEEE Journal of Translational Engineering in Health and Medicine 2, 1–13.

Thulin, C.A., von Essen, C., Zeuchner, E., 1972. Displacements of brain due to positional changes during stereotactic operations. Confin. Neurol. 34 (5), 348–354.

van Dommelen, J.A., van der Sande, T.P., Hrapko, M., Peters, G.W., 2010. Mechanical properties of brain tissue by indentation: interregional variation. J. Mech. Behav. Biomed. Mater. 3 (2), 158–166.

Zappalá, S., Bennion, N.J., Potts, M.R., Wu, J., Kusmia, S., Jones, D.K., Evans, S.L., Marshall, D., 2021. Full-field MRI measurements of in-vivo positional brain shift reveal the significance of intra-cranial geometry and head orientation for stereotactic surgery. Sci. Rep. 11 (1), 17684.

Further reading

DeSesso, J.M., 2009. Functional anatomy of the brain. In: McCandless, D. (Ed.), Metabolic Encephalopathy. Springer, New York, NY.